Journal of Environmental Chemical Engineering 7 (2019) 102910

Contents lists available at ScienceDirect

Journal of Environmental Chemical Engineering

journal homepage: www.elsevier.com/locate/jece

Anion exchange synthesis of hollow β-In_2S_3 nanoparticles: Adsorption and visible light photocatalytic performances

He Li[a], Zhihao Yuan[a], Carla Bittencourt[b], Xiaojiang Li[a], Wei Li[a], Minfang Chen[a], Wenjiang Li[a,*], Rony Snyders[b]

[a] Key Laboratory of Display Materials & Photoelectric Devices, School of Materials Science and Engineering, Tianjin University of Technology, Tianjin 300384, China
[b] Chimie des Interactions Plasma-Surface, University of Mons (Umons), 20 Place du Parc, 7000 Mons, Belgium

ARTICLE INFO

Keywords:
Indium sulfide
Hollow nanoparticles
Ion exchange
Photocatalytsis
Adsorption
Organic dye

ABSTRACT

Crystal phase and morphology control of nano semiconductor materials play a key role on the optimization of their applications. Here, hollow β-In_2S_3 nanoparticles (NPs) with higher surface area were synthesized via an anion exchange process under a hydrothermal condition. The adsorption capacity and photocatalytic activity of the hollow β-In_2S_3 NPs were evaluated using Methylene **blue** (MB) as a model probe both under dark and visible light irradiation. The fast absorption and large adsorption capacity (*ca.* 157.99 mg/g within 60 min) for MB in the solution were associated to the high specific surface area (324.6 m^2/g) of the β-In_2S_3 NPs as well as the electrostatic interaction between the β-In_2S_3 and MB molecule, indicating that adsorption approach plays a crucial role for removing MB from solution. After the adsorption reaction, visible light photocatalytic reaction further degrades the remaining MB in the system. The highest removal efficiency of 100 mg/L of MB solution reached 73.4% under dark for 60 min, and further increased to 92.2% after visible light irradiation for 180 min. The Langmuir isotherm model and pseudo-second-order kinetics were used for the model of the adsorption behavior of MB onto the In_2S_3 sample. The as-prepared hollow In_2S_3 NPs might be anticipated to be used in dye wastewater treatment.

1. Introduction

Water pollution, especially of dye-contaminated water linked to the large-scale development of the textile global industry, has become a substantial matter of concern trigging the research on strategies to remove dyes from contaminated water worldwide [1]. In this context, different nanosized semiconductor materials, including metal oxide and metal sulphide nanomaterials, have been reported as potential active photocatalysts or adsorbents to remove dyes and pigments from contaminated water because of their large specific surface area, unique optical properties, tunable structure and morphology [2,3]. Due to the large energy band gap, metal oxide nanomaterials (TiO_2, ZnO etc.) are only active photocatalysts under ultraviolet (UV) light irradiation because the photons in the visible light range have not high enough energy to excite electrons from the valence band to the conduction band [4,5]. Many methods have been used to change the metal oxide electronic structure for visible light absorption, however, these methods also often create structural defects that accelerate the recombination of photo-generated electron-hole pairs, thus limiting the photocatalytic ability and efficiency [6]. As a contrast, chalcogenides such as ZnSe, ZnTe, and In_2S_3 with narrow energy band gap have shown to be potential active material in light-emitting diodes, optoelectronic devices, solar energy conversion and photocatalysis [7–9]. Up-to-now, various chalcogenides with different morphologies (such as nanotubes, nanorods, nanowires, nanosheets and hollow nanospheres) have been synthesized and used as highly efficient adsorbents/photocatalysts for the removal of organic dyes [10–12]. As a typical III-VI chalcogenide, the stable and non-toxic β-In_2S_3 (up to 420 °C) with a defect spinel lattice, a relatively narrow band gap of 2.0–2.4 eV and a negative potential (approximate -0.9 eV vs. NHE) has been widely studied in the high-efficient adsorbents/photocatalyst [13–15]. For example, as an n-type of semiconductor, In_2S_3 can provide adsorption sites for a strong electrostatic interaction with the cationic dye [16,17]. In the present context, the control of the morphology of nanomaterials has been a key research topic, which plays an important role for improving the performance of different devices [18–20]. In this perspective, owing to their unique physicochemical properties, high density of surface active sites and abundant inner spaces, the interest in the synthesis of hollow nanostructures to be used as delivery vehicles, heterogeneous catalysis and photocatalysis has increased [21]. Recently, reports on hollow β-

* Corresponding author.
E-mail address: liwj@tjut.edu.cn (W. Li).

https://doi.org/10.1016/j.jece.2019.102910
Received 30 November 2018; Received in revised form 15 January 2019; Accepted 16 January 2019
Available online 18 January 2019

In_2S_3 spheres announced their good properties for the degradation of dye in solution [22,23]. For instance, *Rengaraj et al.* [22] reported the high-efficient photodegradation of MB by hollow In_2S_3 microspheres prepared using a thiosemicarbazide-assisted solvothermal process. Nayak et al. [23] found that hollow In_2S_3 microspheres synthesized by a template-free hydrothermal method exhibited remarkable photocatalytic efficiency for the degradation of MB and crystal violet. On the other hand, Cheng et al. [16] and Sharma et al. [17] reported that β-In_2S_3 nanospheres also presented considerable adsorption properties for dyes associated to the electrostatic interaction between dyes and the defects at the In_2S_3 surface. Furthermore, Natarajan et al. [24] pointed out that a higher adsorption capacity of dye on the porous materials could enhance their photocatalytic efficiency. The combination of the adsorption and photocatalytic properties of hollow β-In_2S_3 NPs for the removal of dyes from aqueous solution is a promising strategy for decontamination. So far, besides the traditional templating, coating and chemical etching methods, the ion exchange process has been proved to be an efficient method to create hollow structure, similar to the Kirkendall effect, which is a diffusion phenomenon at the interface between different solids [25–29]. However, there are only few reports on the control of the morphology of In_2S_3 nanostructures by ion exchanging method.

Herein, novel hollow β-In_2S_3 NPs were synthesized via ion exchange under the hydrothermal condition without any surfactant or sacrificial agent. Indium chloride ($InCl_3$) and sodium sulfide (Na_2S) were employed as indium and sulfur sources, respectively. We proposed a novel formation mechanism of hollow β-In_2S_3 NPs, in which $InCl_3$ might be changed to $In(OH)_3$ particles in the solution after an ultrasonic treatment at room temperature [30]. Then, due to the different solubility product constant (K_{sp}) between In_2S_3 and $In(OH)_3$, OH^- anions of $In(OH)_3$ NPs could be replaced by S^{2-} anions from Na_2S under hydrothermal condition, resulting in the formation of hollow In_2S_3 NPs. The detailed structure and optical properties of the synthesized β-In_2S_3 NPs were studied. The fast absorption rate and the maximum adsorption capacity (*ca.* 157.99 mg/g) of β-In_2S_3 sample for 100 mg/L of MB solution in 60 min were associated to the high specific surface area (324.6 m^2/g) and the strong electrostatic interaction between the n-type In_2S_3 and the cationic MB dye, indicating that the adsorption process plays a leading role in the removal of the dye. Moreover, the remaining MB dye in the system after adsorption was further degraded from 73.4% to 92.2% under visible light irradiation for 180 min. Based on the Langmuir isotherm and pseudo-second-order kinetics, the adsorption behavior of MB on In_2S_3 can be considered to be a monolayer adsorption process and is related to the electrostatic interaction [31]. On the basis of experimental observations, the hollow β-In_2S_3 NPs obtained from ion exchange process present a high surface area and negatively charged surface [16,17], which is more beneficial for effectively removing the cationic MB and Rhodamine B (RhB) dyes from solution than for removing the anionic Methyl **orange** (MO) and Congo **red** (CgR) dyes [32,33].

2. Experimental details

2.1. Synthesis of hollow β-In_2S_3 nanoparticles

All purchased chemical reagents are analytical grade and used without further purification. The specific synthesis steps of hollow β-In_2S_3 NPs are as follows: 2.00 mmol of $InCl_3{\cdot}4H_2O$ was dispersed in 20 mL of distilled water at room temperature with continuous magnetic stirring and ultrasonic treatment for 30 min to form the homogeneous suspension of $In(OH)_3$ NPs [30]. Then, 20 mL of Na_2S solution containing 5.00 mmol of $Na_2S{\cdot}9H_2O$ was added dropwise to the $In(OH)_3$ suspension. After magnetic stirring for 30 min, a homogeneous pale yellow suspension was obtained. The pale yellow precursor solution was transferred into an autoclave, and heated in a bake oven at 180 °C for 12, 18 and 24 h, respectively. After cooling to room temperature, the autoclave was opened, and the obtained products were centrifuged and washed several times successively with distilled water and ethanol. The yellow precipitates were dried in a vacuum oven at 70 °C for 6 h and labelled as IS-1, IS-2 and IS-3, corresponding to reaction time of 12, 18 and 24 h, respectively.

2.2. Characterization of β-In_2S_3 nanoparticles

X-ray diffraction (XRD) patterns obtained on an X-ray diffractometer (D/Ma x 2500 pc) using Cu Kα irradiation were used to determine the phase constitution of the prepared samples (Scan rate: 0.02° s^{-1}, Accelerating voltage: 40 Kv, and Applied current: 150 mA). Surface composition and electronic states were investigated by energy dispersive spectroscopy (EDS) and X-ray photoelectron spectroscopy (XPS, ESCALAB 250Xi with Al-Kα source at a power of 180 W (15 kV × 12 mA)). The morphology of samples was studied by field-emission scanning electron microscope (FESEM, ZEISS MERLIN Compact) and transmission electron microscopy (TEM, Talos F 200 X). The specific BET surface area (S_{BET}) was calculated by following the nitrogen adsorption-desorption and Brunnauer-Emmet-Teller method using an automated surface area and pore size analyzer (TriStar II 3020 with analysis bath tempeture: -195.850 °C, warm free space: 11.5981 cm^3 measured, equilibration interval: 5 s, and sample density: 1.000 g/cm^3). UV–vis spectra and diffuse reflectance spectra (DRS) were recorded on a TU-1980 spectrometer equipped with an integrating sphere attachment. In UV–vis DRS, $BaSO_4$ was used as the reflectance standard.

2.3. Adsorption and photocatalysis evaluation of β-In_2S_3 nanoparticles

The photocatalytic activity of the In_2S_3 sample was evaluated by the degradation of MB solution (100 mg/L) under visible light irradiation (300 W Xenon lamp with a 420 nm cut-off filter). Typically, 40 mg of IS-X (X = 1, 2 or 3) sample was dispersed in 80 ml of MB aqueous solution as the photocatalytic reactor. Then, the reactor was put into a dark room under vigorous stirring for 60 min to ensure the establishment of an adsorption-desorption equilibrium. After adsorption, the mixed suspension was exposed under visible light irradiation for 180 min. At given intervals of time, 3 mL of the mixed suspension was extracted and centrifuged to remove the adsorbent. UV–vis spectroscopy was used to monitor the concentration of the MB solution by measuring the intensity of the MB characteristic absorption at 664 nm. As a contrast, the adsorption property of IS-X (X = 1, 2 or 3) sample for 100 mg/L of MB solution were carried out under dark for 240 min. Meanwhile, the adsorption capacity and the adsorption mechanism were detailed studied in the Supporting Information.

3. Results and discussion

3.1. Formation mechanism of hollow In_2S_3 nanoparticles

The formation of the hollow structured In_2S_3 NPs can be associated to the different solubility product constant (K_{sp}) of $In(OH)_3$ (1.4×10^{-33}) and In_2S_3 (6.3×10^{-36}). At the onset of the reaction process, the $In(OH)_3$ particles formed by the hydrolysis of In^{3+} in aqueous solution can be considered as a template [30]. Due to the large disparity of K_{sp}, anion exchange following the Kirkendall effect is promoted between OH^- and S^{2-} anions [28,29], resulting in the formation of In_2S_3 hollow nanostructure. The schematic illustration of the formation mechanism of the hollow structured In_2S_3 NPs is shown in Fig. 1, and the detail chemical reactions are as follow:

$$\mathrm{In}^{3+} + 3H_2O \Leftrightarrow \mathrm{In}(OH)_3 + 3H^+ \quad (1)$$

$$\mathrm{In}(OH)_3 \Leftrightarrow \mathrm{In}^{3+} + 3OH^- \quad (2)$$

$$\mathrm{In}_2S_3 \Leftrightarrow 2\,\mathrm{In}^{3+} + 3S^{2-} \quad (3)$$

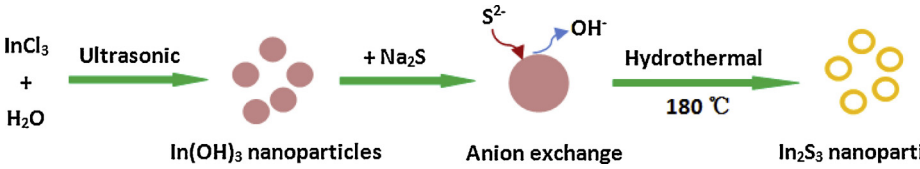

Fig. 1. Schematic illustration of the synthesis and formation mechanism of hollow In_2S_3 nanoparticles.

$$3S^{2-} + 2\ln(OH)_3 \Rightarrow \ln_2S_3 + 6OH^- \quad (4)$$

Firstly, $In(OH)_3$ particles are formed via the sonication of $InCl_3$ aqueous solution at room temperature (Eq. (1)), then there is a weak chemical equilibrium between $In(OH)_3$ particles and OH^- ions (Eq. (2)). Based on the Kirkendall effect, after adding Na_2S solution into the $In(OH)_3$ suspension, mutual diffusion occurs of OH^- (outward diffusion) on the surface of $In(OH)_3$ particles and S^{2-} (inward diffusion) following the Eqs. (2) and (3). S^{2-} ions in the solution diffuse inward through the interfacial shell and react with In^{3+} ions to form In_2S_3 nuclei which precipitated on the surface of $In(OH)_3$ NPs. The latter therefore act as a template in the formation process. The OH^- anions presenting on the surface of the $In(OH)_3$ particles are gradually replaced by S^{2-} anions (Eq. (4)), finally forming hollow In_2S_3 nanostructures.

3.2. Structure and composition

The crystal structure of In_2S_3 samples prepared under different reaction time was characterized by XRD as shown in Fig. 2. The observed main diffraction peaks at 2θ = 27.4°, 33.3°, 43.7° and 47.8° can be indexed to the (311), (400), (511) and (440) planes of the cubic In_2S_3 phase (JCPDS card No. 65-0459, a = 10.774 Å), similar to previous report [31]. No impurity phases such as InS, In_2O_3, and $In(OH)_3$ are observed. Upon increasing the hydrothermal reaction time, the intensity and shape of diffraction peaks, especially (311) plane, sharpen and strengthen, revealing the well crystalline structure and large size of the In_2S_3 nanocrystals [34]. Corresponding to the (311) reflection peak, the average grain sizes were calculated using the Scherrer formula to be *ca*. 5.1 nm, 5.7 nm and 6.9 nm for IS-1, IS-2 and IS-3, respectively [35]. Moreover, the relative intensities of (400) peak to (311) peak (I_{400}/I_{311}) and (440) peak to (311) peak (I_{440}/I_{311}) of In_2S_3 (**Table S1**) are much higher than that of the standard diffraction pattern, implying that the as-prepared In_2S_3 samples grown preferentially along the (400) and (440) directions [18,36].

The typical XPS spectra recorded on the IS-2 sample are shown in Fig. 3. The XPS survey spectrum in Fig. 3**A** reveals that the sample is mainly composed of In and S element. The traces of C and O observed in the survey spectra might be originated from H_2O, O_2 and CO_2 adsorbed on the surface of the sample due to exposure to the air [37]. In the high energy resolution XPS spectrum recorded on the In element region (Fig. 3B), two high intensity peaks are observed at 445.1 eV and 452.6 eV can be attributed to photoelectrons emitted from the In $3d_{5/2}$ and In $3d_{3/2}$ levels, corresponding to In^{3+} oxidation state of In_2S_3 [34]. The asymmetry in the In 3d peaks can be fitted by a doublet with components located at 443.8 eV and 451.3 eV, indicating the presence of $In(OH)_3$ phase. The absence of $In(OH)_3$ in the XRD suggests that the $In(OH)_3$ phase is localized on the sample surface, in accordance with the results reported by Zhang et al [38]. The two high-intensity peaks at 161.5 eV and 162.7 eV in the high energy resolution spectrum recorded in the S region (Fig. 3C) correspond to the photoemission from the S $2p_{3/2}$ and S $2p_{1/2}$ levels of S^{2-} in the In_2S_3 lattice, respectively [23]. The low intensity components at 161.3 eV and 160.1 eV can be associated with an S-rich state for the obtained products, indicating the existence of negatively charged defect points in In_2S_3 sample because of the lack of positively charged In^{3+} ions in the lattice, resulting in the formation of the negatively charged surface [20].

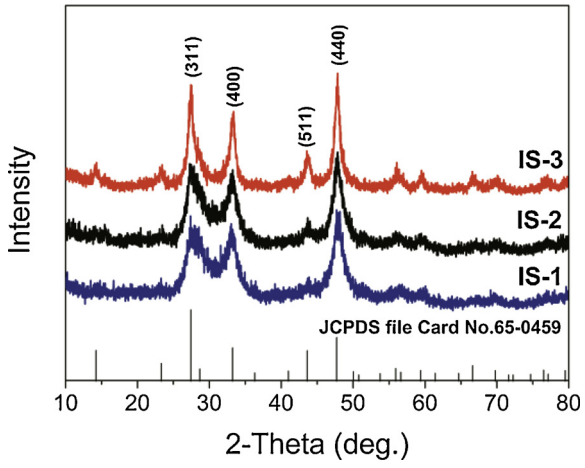

Fig. 2. XRD patterns of the as-prepared In_2S_3 samples.

3.3. Morphology

SEM images of the In_2S_3 samples obtained under different reaction time are shown in **Fig. S1**. It can be observed that the In_2S_3 samples are composed of aggregated NPs with a narrow size distribution. The average particle sizes of IS-1, IS-2 and IS-3 samples, estimated by Nano measure software [39], gradually increased from 18.7 nm, 23.0 nm to 38.2 nm, suggesting that the hydrothermal reaction time has a significant effect on the size of In_2S_3 NPs [40]. Moreover, EDS pattern shown in **Fig. S1-D** reveals that the sample consists primarily of In and S, and the atomic ratio of In to S is about 1:1.51, in accordance with the XPS results.

Fig. 4 shows typical TEM micrographs, the contrast between the dark edges and lighter central regions in Fig. 4**A** and **B** indicates that the In_2S_3 NPs actually have a hollow structure. According to the TEM observations, the yield of hollow particles of In_2S_3 sample is over 80%. From the high-resolution TEM image (HRTEM) (Fig. 4C) taken at the wall edges of hollow In_2S_3 NPs (marked by the white circle in Fig. 3B), parallel lattice fringes can be observed, and the interplanar distance of 0.27 nm corresponded to the (400) lattice plane of cubic β-In_2S_3 [18]. The selected area electron diffraction (SAED) marked by the white circle is shown in Fig. 4D, the regular circular diffraction rings suggest that the hollow In_2S_3 NPs possess polycrystalline structure [10]. Moreover, the (311), (400) and (440) plane are obviously observed in the SAED pattern, consistent with the diffraction peaks in the XRD patterns.

3.4. BET measurements

The surface area and pore size distribution of In_2S_3 hollow-structured NPs were measured by N_2 adsorption-desorption isotherm and the BJH method as displayed in Fig. 5. The isotherm patterns can be categorized as a type IV isotherm with H2 hysteresis loop in the range of 0.4–1.0 P/P_0, indicating the presence of mesoporous structure according to the International Union of Pure and Applied Chemistry (IUPAC) classification [41]. The pore size distribution (the inset in Fig. 5) obtained from the desorption branch of the isotherm is broad, and mainly around from 1.5 nm to 15 nm with a unimodal shape at 4.0 nm, which is in agreement with the particle size obtained from TEM

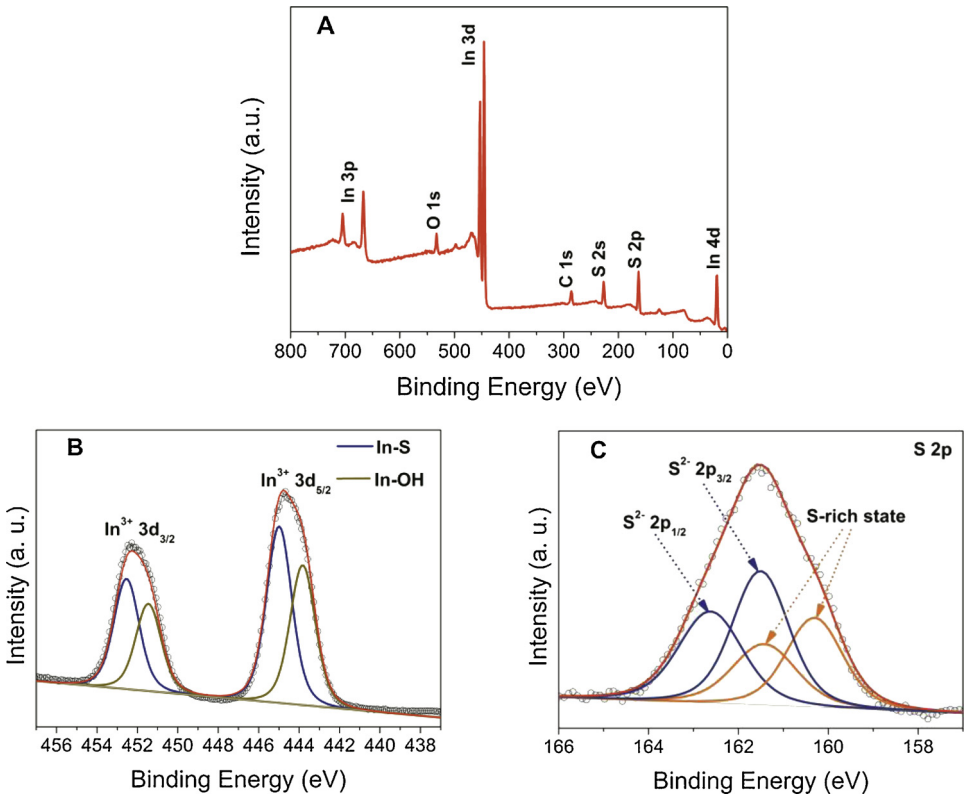

Fig. 3. XPS spectra of sample IS-2: (A) survey, (B) In 3d and (C) S 2p.

analysis. The calculated surface area and average pore diameter of samples IS-1, IS-2 and IS-3 are presented in **Table S2**. The results indicate that the sample IS-2 has the largest surface area of 324.6 m^2/g, much higher than previously reported In_2S_3 hollow sphere of 47.4 m^2/g and 130.7 m^2/g [22,23]. The large surface area and porous structure of IS-2 are beneficial to remove a large amount of dye molecules in the solution [42].

3.5. Optical properties

Fig. 6**A** shows the UV–vis DRS of the hollow In_2S_3 NPs in the wavelength range of 200–800 nm. The similar absorption curve with wide and intense absorption peak from 200 to 700 nm indicates that as-prepared In_2S_3 possesses a strong absorption in the ultraviolet light and visible light regions. Besides, the steep shape of the absorption band suggests that the visible light absorption of In_2S_3 NPs is due to the transition of electrons from the valence band to the conduction band, which can be the evidence of the narrow size distribution, uniform crystallites and high phase purity [22].

From these data, the energy band gap can be calculated by extrapolation of the linear portion of the $(\alpha h\upsilon)^2$ *vs.* $h\upsilon$ plots to $\alpha = 0$ (Fig. 6B), using equation:

$$(\alpha h\upsilon)^2 = A(h\upsilon - E_g)$$

where α, $h\upsilon$, and E_g are the absorption coefficient, the discrete photon energy, and the band gap energy, respectively. A is a constant [43]. The energy band gaps of samples IS-1, IS-2 and IS-3 were calculated to be *ca.* 2.15, 2.13 and 2.27 eV, respectively, which is in good agreement with the reported value (2.0–2.3 eV) [23]. These results reveal that the size and surface area of In_2S_3 NPs resulting from the different reaction

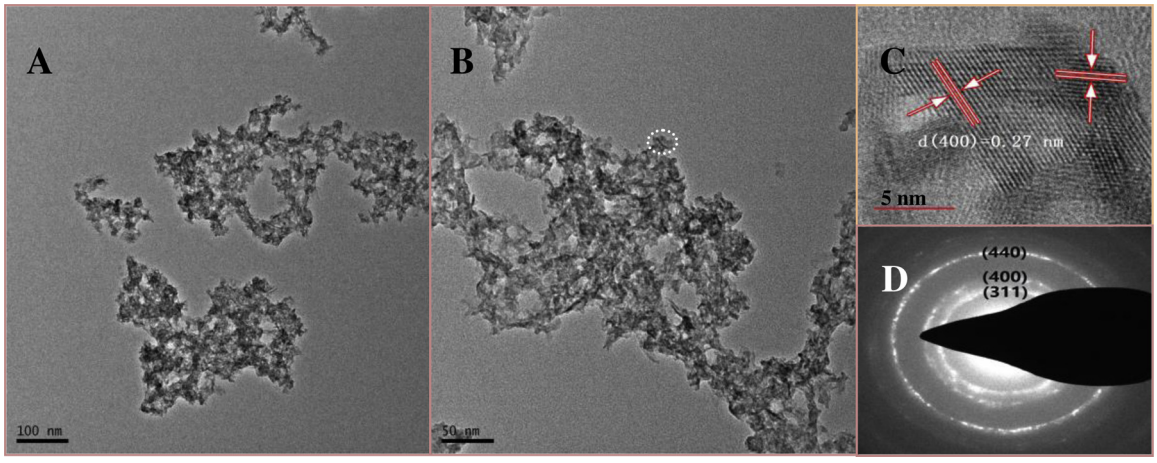

Fig. 4. (A and B) TEM images, (C) high-resolution TEM image, and (D) SAED image of IS-2 sample.

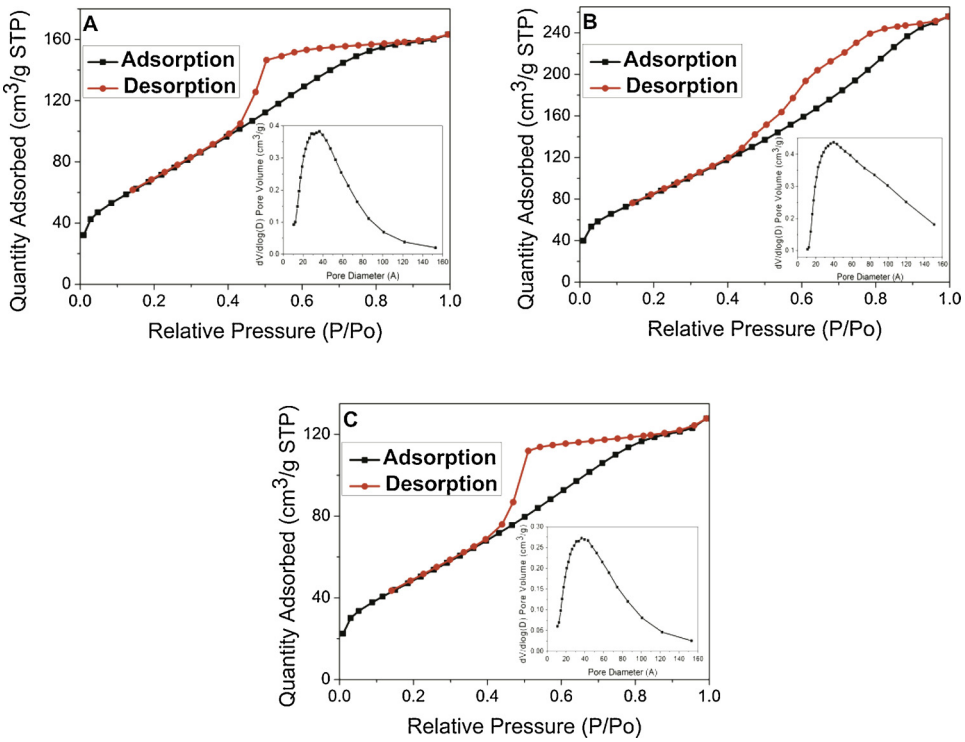

Fig. 5. Nitrogen adsorption-desorption curves: (A) IS-1, (B) IS-2 and (C) IS-3; pore size distribution curves (inset).

time have a significant effect on their optical properties. Meanwhile, IS-2 sample exhibits the strongest visible light absorption, showing a suitable visible light-driven photocatalyst for the degradation of organic dye.

3.6. Adsorption and photocatalysis

In the primary adsorption experiments, we found that MB molecules in low concentration solution was nearly completely adsorbed by In_2S_3 product in the dark condition, and the solution became clear, indicating no meaning to further identify the photodegradation efficiency. Therefore, the concentrated MB solution (100 mg/L) was used as the model wastewater to be studied in the photocatalytic experiments. Fig. 7**A** shows the absorbance variation of MB solution as a function of time in the presence of IS-2 sample combining adsorption and photocatalysis. The intensity of the absorbance peak of MB sharply decreased in the dark period suggesting that most of the dye had been adsorbed. After the adsorption, the intensity of absorbance peak of MB further decreased gradually under visible light irradiation, demonstrating the decomposition of the remaining MB dye molecules in the system. From Fig. 7B, the removal% for MB by IS-1, IS-2 and IS-3 after adsorption for 60 min under dark (adsorption-desorption equilibrium) are calculated to be *ca.* 64.8%, 73.4% and 50.2%, respectively. No more MB dye was adsorbed further increasing the adsorption time to 240 min (**Fig. S2**). The more removal rate appearing in the adsorption process might be attributed to the strong electrostatic interaction between the dye and catalyst because In_2S_3 is an n-type semiconductor material and MB is a cationic dye [16,17,44]. After adsorption-desorption equilibrium, the overall removal of MB onto IS-1, IS-2 and IS-3 under visible light irradiation for 180 min further increased to 82.8%, 92.2% and 63.7%, respectively, indicating that the photocatalytic efficiency under visible light is very significant. Additionally, the photodegradation rate and the corresponding reaction kinetics (k) were presented in Table 1. The sample IS-2 exhibits the most efficient photodegradation of 70.8% with the highest k value of 0.0060 min^{-1}, indicating that the surface area and the hollow structure might support more defect sites and active sites, which is beneficial for dark adsorption and visible light photocatalysis of MB in the solution [17,45].

Based on the above experimental analysis, it can be found that the adsorption process plays an important role for removing organic dye. In this context, a series of adsorption experiments of different dyes on IS-2 sample were carried out, in which another cationic RhB dye and two

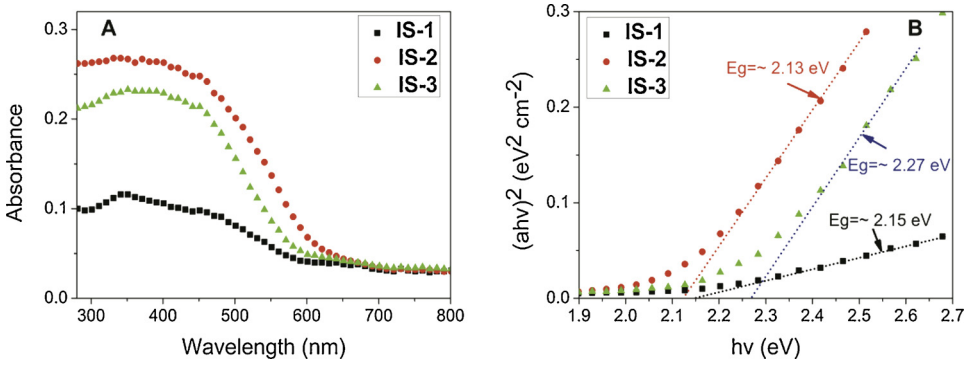

Fig. 6. (A) UV–vis diffuse reflectance spectra and (B) band gaps of In_2S_3 hollow nanoparticles.

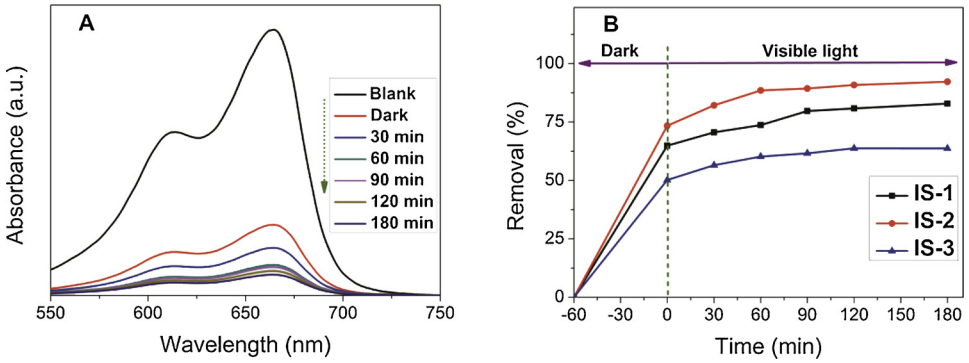

Fig. 7. (A) Absorbance variation of MB solution with time using IS-2 sample as photocatalyst under dark and visible light. (B) Removal% of MB on In_2S_3 by adsorption and photocatalytic process.

Table 1
Adsorption capacity, removal/photocatalytic efficiency, and rate constant of 100 mg/L MB solution onto hollow In_2S_3 nanoparticles.

Sample	Adsorption capacity (mg/g)	Photocatalytic efficiency (%)	Rate constant (k)[α] (min^{-1})	Overall removal efficiency (dark + light) (%)
IS-1	129.6	51.2	0.0041	82.8
IS-2	146.8	70.8	0.0060	92.2
IS-3	100.4	27.1	0.0017	63.7

[α] Calculated by the pseudo-first-order reaction kinetics equation: $\ln(C/C_0) = -k_1 t$ [3].

anionic dyes (MO and CgR) were chosen as the pollutants while the other parameters were kept unchanged. As shown in **Fig. S3**, the adsorption capacity of IS-2 sample for MO (23.46 mg/g) and CgR (43.83 mg/g) is much lower than that of RhB (100.22 mg/g) and MB (157.99 mg/g), revealing that the electrostatic interaction between absorbent and dye molecules is favorable for the enhanced adsorption performance [21]. Besides, the adsorption capacity of IS-2 sample for RhB is lower than that of MB dye, which might be associated with the different negative adsorption energy and chromophoric structure of dyes [46]. This result indicates that the hollow In_2S_3 NPs can efficiently and selectively adsorb organic dyes, which provides a useful guidance for the photocatalytic degradation of organic dyes of In_2S_3 catalyst [47]. Furthermore, in order to accurately evaluate the adsorption capacity and adsorption mechanism of MB onto In_2S_3, IS-2 sample was used as the representative adsorbent to different initial concentration of MB solution (50, 100, 150, 200 mg/L). The corresponding adsorption% and adsorption capacity are shown in **Fig. S4** and **Table S3**. The adsorption speed of the dye is very fast, for the 50 mg/L of MB solution, nearly 100% of MB adsorbed on the particles within 5 min. Upon increasing the dye initial concentration, the adsorption behaviour of the hollow β-In_2S_3 for MB repeats the analogous initial fast uptake, almost invariable after 60 min. The calculated maximum adsorption capacity (*ca.* 157.99 mg/g) is very close to the theoretical value from the pseudo-second-order model and Langmuir isotherm with better correlation coefficient (R^2), indicating that the adsorption process of MB onto In_2S_3 likely takes place via monolayer molecular adsorption with the rate-limiting step of chemisorptions (**Fig. S5-S6 and Table S3-S4**).

3.7. Photocatalytic mechanism

In order to further understand the photocatalytic mechanism of In_2S_3 for MB dye, the valence band (VB) and conduction band (CB) potentials (E_{CB} and E_{VB}) of the hollow β-In_2S_3 NPs (IS-2) at the point of zero charge have been estimated by the Mulliken equation [46]:

$$E_{VB} = \chi - E_c + 0.5E_g$$

$$E_{CB} = E_{VB} - E_g$$

where E_g = 2.13 eV, χ is the electronegativity of the In_2S_3 (~ 4.69 eV), E_c is the energy of free electrons on the hydrogen scale (~ 4.5 eV). The calculated values of E_{CB} and E_{VB} are *ca.* -0.87 eV and 1.26 eV, respectively. As presented in Fig. 8, the E_{VB} of In_2S_3 sample was more negative than the E ($^{\cdot}OH/OH^-$) of 2.38 eV and E ($^{\cdot}OH/H_2O$) of 2.27 eV, suggesting that the photogenerated holes could not convert H_2O to $^{\cdot}OH$ and H^+ [48,49]. Instead, they could directly oxidize the dye molecules into final products [32]. Further, the E_{CB} of In_2S_3 was more negative than E ($O_2/^{\cdot}O_2^-$) of -0.28 eV, so the photogenerated electrons could react with molecular O_2 absorbed on the surface of In_2S_3 photocatalyst to generate $^{\cdot}O_2^-$ under visible light irradiation [50]. Finally, the organic dye was converted to small molecules and even CO_2 and H_2O by $^{\cdot}O_2^-$ and h^+. Therefore, the $^{\cdot}O_2^-$ and h^+ act as the main active species in the photocatalytic reaction, in agreement with the results of the previous report [51].

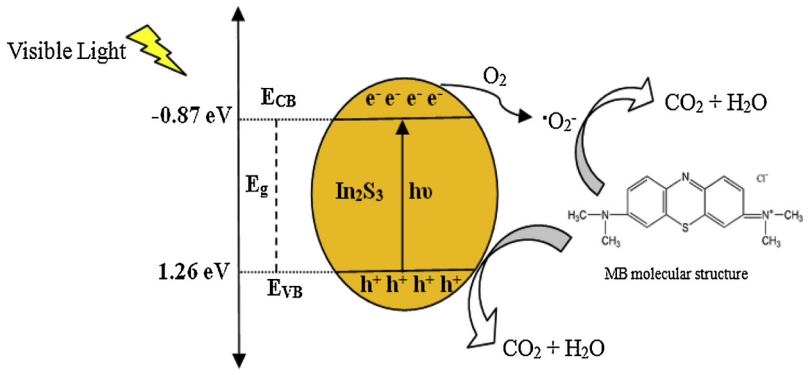

Fig. 8. Schema of the model for the excitation and charge transfer processes of In_2S_3 driven by visible light.

4. Conclusions

Hollow-structured β-In_2S_3 NPs, with a high surface area of 324.6 m^2/g, were synthesized via an anion exchange process, which exhibited highly efficient removal of concentrated MB dye combining dark adsorption and visible light photocatalytic degradation. The highest removal efficiency reached 73.4% by adsorption under dark for 60 min, and further increased to 92.2% after visible light irradiation for 180 min. We observed that the adsorption of dye plays a dominant role in its removal. The enhanced photocatalytic performance observed for the hollow-structured β-In_2S_3 NPs can be associated to the unique structure and large surface area providing a high density of chemically active sites, higher light-harvesting efficiency, and larger adsorption capacity of the dye. Evidently, hollow β-In_2S_3 NPs might be exploited for water remediation and many other environmental applications.

Acknowledgements

This work was supported by the Joint Foundation of National Natural Science Foundation of China (Grant No. U1764254), China; 321 Talent Project of Nanjing (Grant No. 631783), China; and 111 Project (Grant No. D17003), China.

Appendix A. Supplementary data

Supplementary material related to this article can be found, in the online version, at doi:https://doi.org/10.1016/j.jece.2019.102910.

References

[1] X.W. Liu, J.J. Xu, Z.Y. Ni, R.C. Wang, J.H. You, R. Guo, Adsorption and visible-light-driven photocatalytic properties of Ag_3PO_4/WO_3 composites: A discussion of the mechanism, Chem. Eng. J. 356 (2019) 22–33, https://doi.org/10.1016/j.cej.2018.09.001.

[2] R.B. Wei, Z.L. Huang, G.H. Gu, Z. Wang, L.X. Zeng, Y.B. Chen, Z.Q. Liu, Dual-co-catalysts decorated rimous CdS spheres advancing highly-efficient visible-light photocatalytic hydrogen production, Appl. Catal. B-Environ. 231 (2018) 101–107, https://doi.org/10.1016/j.apcatb.2018.03.014.

[3] X.W. Liu, W.Q. Yang, C.Q. Yu, H.H. Zhang, Influence of TiO_2 morphology on adsorption-photocatalytic efficiency of TiO_2-graphene composites for methylene blue degradation, J. Environ. Chem. Eng. 6 (2018) 4899–4907, https://doi.org/10.1016/j.jece.2018.07.009.

[4] C.J. Páez, P.S. Cid, J.A. Navío, M.C. Hidalgo, A comparative assessment of the UV-photocatalytic activities of ZnO synthesized by different routes, J. Environ. Chem. Eng. 6 (2018) 7161–7171, https://doi.org/10.1016/j.jece.2018.11.004.

[5] Q.Y. Tian, W.J. Yao, W. Wu, C.Z. Jiang, NIR-light activated upconversion semiconductor photocatalysts, Nanoscale Horiz. 4 (2019) 10–25, https://doi.org/10.1039/C8NH00154E.

[6] Z.B. Yu, X.Q. Chen, X.D. Kang, Y.P. Xie, H.Z. Zhu, S.L. Wang, S. Ullah, H. Ma, L.Z. Wang, G. Liu, X.L. Ma, H.M. Cheng, Noninvasively modifying band structures of wide-bandgap metal oxides to boost photocatalytic activity, Adv. Mater. 30 (2018), https://doi.org/10.1002/adma.201706259 e1706259.

[7] X. Wu, R. Xu, R.J. Zhu, R. Wu, B. Zhang, Converting 2D inorganic-organic ZnSe-DETA hybrid nanosheets into 3D hierarchical nanosheet-based ZnSe microspheres with enhanced visible-light-driven photocatalytic performances, Nanoscale 7 (2015) 9752–9759, https://doi.org/10.1039/c5nr02329g.

[8] K.S. Lee, G. Oh, E.K. Kim, High performance intermediate-band solar cells based on ZnTe:Cr with ZnO:Al electron transport layer, Sol. Energy 164 (2018) 262–266, https://doi.org/10.1016/j.solener.2018.02.074.

[9] M. Li, X.L. Tu, Y.J. Su, J. Lu, J. Hu, B.F. Cai, Z.H. Zhou, Z. Yang, Y.F. Zhang, Controlled growth of vertically aligned ultrathin In_2S_3 nanosheet arrays for photoelectrochemical water splitting, Nanoscale 10 (2018) 1153–1161, https://doi.org/10.1039/c7nr06182j.

[10] Z.B. Wu, X.Z. Yuan, G.M. Zeng, L.B. Jiang, H. Zhong, Y.C. Xie, H. Wang, X.H. Chen, H. Wang, Highly efficient photocatalytic activity and mechanism of Yb^{3+}/Tm^{3+} codoped In_2S_3 from ultraviolet to near infrared light towards chromium (VI) reduction and rhodamine B oxydative degradation, Appl. Catal. B-Environ. 225 (2018) 8–21, https://doi.org/10.1016/j.apcatb.2017.11.040.

[11] H.J. Wang, Y. Cao, L.L. Wu, S.S. Wu, A. Raza, N. Liu, J.Y. Wang, ZnS-based dual nano-semiconductors (ZnS/PbS, ZnS/CdS or ZnS/Ag_2S,): a green synthesis route and photocatalytic comparison for removing organic dyes, J. Environ. Chem. Eng. 6 (2018) 6771–6779, https://doi.org/10.1016/j.jece.2018.10.034.

[12] D.P. Kumar, H. Park, E.H. Kim, S. Hong, M. Gopannagari, D.A. Reddy, T.K. Kim, Noble metal-free metal-organic framework-derived onion slice-type hollow cobalt sulfide nanostructures: enhanced activity of CdS for improving photocatalytic hydrogen production, Appl. Catal. B-Environ. 224 (2018) 230–238, https://doi.org/10.1016/j.apcatb.2017.10.051.

[13] S.B. Kokane, R. Sasikala, D.M. Phase, S.D. Sartale, In_2S_3 nanoparticles dispersed on g-C_3N_4 nanosheets: role of heterojunctions in photoinduced charge transfer and photoelectrochemical and photocatalytic performance, J. Mater. Sci. 52 (2017) 7077–7090, https://doi.org/10.1007/s10853-017-0940-x.

[14] R.S. Becker, T. Zheng, J. Elton, M. Saeki, Synthesis and photoelectrochemistry of In_2S_3, Sol. Energy Mater. 13 (1986) 97–107, https://doi.org/10.1016/0165-1633(86)90038-9.

[15] Y. Liu, H. Xu, Y. Qian, Double-source approach to In_2S_3 single crystallites and their electrochemical properties, Cryst. Growth Des. 6 (2006) 1304–1307, https://doi.org/10.1021/cg0504298.

[16] Y. Cheng, H.L. Niu, J.S. Chen, J.M. Song, C.J. Mao, S.Y. Zhang, C.L. Chen, Y.H. Gao, Highly stable hierarchical flower-like β-In_2S_3 assembled from 2D nanosheets with high adsorption-photodecolorization activities for the treatment of wastewater, J. Nanopart. Res. 19 (2017), https://doi.org/10.1007/s11051-017-3858-y e166.

[17] R.K. Sharma, Y.N. Chouryal, S. Chaudhari, J. Saravanakumar, S.R. Dey, P. Ghosh, Adsorption-driven catalytic and photocatalytic activity of phase tuned In_2S_3 nanocrystals synthesized via ionic liquids, ACS Appl. Mater. Interfaces 13 (2017) 11651–11661, https://doi.org/10.1021/acsami.7b01092.

[18] J. Chen, W.X. Liu, W.W. Gao, Tuning photocatalytic activity of In_2S_3 broadband spectrum photocatalyst based on morphology, Appl. Surf. Sci. 368 (2016) 288–297, https://doi.org/10.1016/j.apsusc.2016.02.008.

[19] Y. Wu, C. Wadia, W.L. Ma, B. Sadtler, A.P. Alivisatos, Synthesis and photovoltaic application of copper(I) sulfide nanocrystals, Nano Lett. 8 (2008) 2551–2555, https://doi.org/10.1021/nl801817d.

[20] T. Berestok, P. Guardia, J.B. Portals, S. Estrade, J. Llorca, F. Peiro, A. Cabot, S.L. Brock, Surface chemistry and nano-/microstructure engineering on photocatalytic In_2S_3 nanocrystals, Langmuir 34 (2018) 6470–6479, https://doi.org/10.1021/acs.langmuir.8b00406.

[21] S.L. Yang, Z.H. Wu, L.P. Huang, B.H. Zhou, M. Lei, L.L. Sun, Q.Y. Tian, J. Pan, W. Wu, H.B. Zhang, Significantly enhanced dye removal performance of hollow tin oxide nanoparticles via carbon coating in dark environment and study of its mechanism, Nanoscale Res. Lett. 9 (2014) 442–450, https://doi.org/10.1186/1556-276X-9-442.

[22] S. Rengaraj, S. Venkataraj, C.W. Tai, Y.H. Kim, E. Repo, M. Sillanpaa, Self-Assembled mesoporous hierarchical-like In_2S_3 hollow microspheres composed of nanofibers and nanosheets and their photocatalytic activity, Langmiur 27 (2011) 5534–5541, https://doi.org/10.1021/la104780d.

[23] A.K. Nayak, S. Lee, Y. Sohn, D. Pradhan, Synthesis of In_2S_3 microspheres using a template-free and surfactant-less hydrothermal process and their visible light photocatalysis, CrystEngComm 16 (2014) 8064–8072, https://doi.org/10.1039/c4ce00836g.

[24] S. Natarajan, H.C. Bajaj, R.J. Tayade, Recent advances based on the synergetic effect of adsorption for removal of dyes from waste water using photocatalytic process, J. Environ. Sci. China (China) 65 (2018) 201–222, https://doi.org/10.1016/j.jes.2017.03.011.

[25] Q. Wang, J.X. Li, G.D. Li, Formation of CuS nanotube arrays from CuCl nanorods through a gas-solid reaction route, J. Cryst. Growth 299 (2007) 386–392, https://doi.org/10.1016/j.jcrysgro.2006.11.304.

[26] L. Ye, C. Wu, W. Guo, MoS_2 hierarchical hollow cubic cages assembled by bilayers: one-step synthesis and their electrochemical hydrogen storage properties, Chem. Commun. (Camb.) 45 (2006) 4738–4740, https://doi.org/10.1039/b610601c.

[27] Y.L. Wang, L. Cai, Y.N. Xia, Monodisperse spherical colloids of Pb and their use as chemical templates to produce hollow particles, Adv. Mater. 17 (2005) 473–477, https://doi.org/10.1002/adma.200401416.

[28] A.A. El Mel, R. Nakamura, C. Bittencourt, The Kirkendall effect and nanoscience: hollow nanospheres and nanotubes, Beilstein J. Nanotechnol. 6 (2015) 1348–1361, https://doi.org/10.3762/bjnano.6.139.

[29] Y.D. Yin, R.M. Rioux, C.K. Erdonmez, S. Hughes, G.A. Somorjai, A. PaulAlivisatos, Formation of hollow nanocrystals through the nanoscale Kirkendall effect, Science 304 (2004) 711–714, https://doi.org/10.1126/science.1096566.

[30] S. Avivi, Y. Mastai, A. Gedanken, Sonohydrolysis of In^{3+} Ions: Formation of needlelike particles of indium hydroxide, Chem. Mater. 12 (2000) 1229–1233, https://doi.org/10.1021/cm9903677.

[31] L.N. Zhang, W. Zhang, H.B. Yang, W.Y. Fu, M.H. Li, H. Zhao, J.W. Ma, Hydrothermal synthesis and photoelectrochemical properties of In_2S_3 thin films with a wedge like structure, Appl. Surf. Sci. 258 (2012) 9018–9024, https://doi.org/10.1016/j.apsusc.2012.05.141.

[32] Z.F. Jiang, J.M. Xie, D.L. Jiang, Z.X. Yan, J.J. Jing, D. Liu, Enhanced adsorption of hydroxyl contained/anionic dyes on nonfunctionalized Ni@SiO_2 core-shell nanoparticles: Kinetic andthermodynamic profile, Appl. Surf. Sci. 292 (2014) 301–310, https://doi.org/10.1016/j.apsusc.2013.11.136.

[33] Q.D. Qin, J. Ma, K. Liu, Adsorption of anionic dyes on ammonium-functionalized MCM-41, J. Hazard. Mater. 162 (2009) 133–139, https://doi.org/10.1016/j.jhazmat.2008.05.016.

[34] L.Y. Chen, Z.D. Zhang, W.Z. Wang, Self-assembled porous 3D flowerlike beta-In_2S_3 structures: synthesis, characterization, and optical properties, J. Phys. Chem. C 11 (2008) 4117–4123, https://doi.org/10.1021/jp710074h.

[35] A. Modwi, M.A. Abbo, E.A. Hassan, O.K. Al-Duaij, A. Houas, Adsorption kinetics and photocatalytic degradation of malachite green (MG) via Cu/ZnO nanocomposites, J. Environ. Chem. Eng. 5 (2017) 5954–5960, https://doi.org/10.1016/j.jece.2017.11.024.

[36] C.Y. Wei, W. Guo, J.Q. Yang, H.M. Fan, J. Zhang, W.J. Zheng, Facile solvothermal synthesis of 3D flowerlike β-In_2S_3 microspheres and their photocatalytic activity performance, RSC Adv. 4 (2014) 50456–50463, https://doi.org/10.1039/c4ra08545k.

[37] X.J. Li, Y.N. Li, F. Xie, W. Li, W.J. Li, M.F. Chen, Y. Zhao, Preparation of monodispersed CuS nanocrystals in an oleic acid/paraffin system, RSC Adv. 5 (2015) 84465–84470, https://doi.org/10.1039/c5ra18475d.
[38] F. Zhang, X.Y. Li, Q.D. Zhao, A.C. Chen, Facile and controllable modification of 3D In_2O_3 microflowers with In_2S_3 nanoflakes for efficient photocatalytic degradation of gaseous ortho-dichlorobenzene, J. Phys. Chem. C 120 (2016) 19113–19123, https://doi.org/10.1021/acs.jpcc.6b03618.
[39] Z.Y. Chen, A.R. Wang, W. Sun, C. Wang, L. Kong, F. Li, X.H. Tian, S.L. Li, J.Y. Wu, Y.P. Tian, Synthesis, nonlinear optical properties and cellular imaging of hybrid ZnS nanoparticles capped with conjugated terpyridine derivatives, J. Mater. Sci. 53 (2018) 1798–1800, https://doi.org/10.1007/s10853-017-1621-5.
[40] C.A. Chiu, K.D. Hristovski, R. Dockery, K. Doudrick, P. Westerhoff, Modeling temperature and reaction time impacts on hematite nanoparticle size during forced hydrolysis of ferric chloride, Chem. Eng. J. 210 (2012) 357–362, https://doi.org/10.1016/j.cej.2012.08.093.
[41] M.Q. Yang, B. Weng, Y.J. Xu, Improving the visible light photoactivity of In_2S_3-graphene nanocomposite via a simple surface charge modification approach, Langmuir 33 (2013) 10549–10558, https://doi.org/10.1021/la4020493.
[42] J. Wang, H.X. Zhong, Z.L. Wang, F.L. Meng, X.B. Zhang, Integrated three-dimensional carbon paper/carbon tubes/cobalt-sulfide sheets as a bifunctional electrode for overall water splitting, ACS Nano 10 (2016) 2342–2351, https://doi.org/10.1021/acsnano.5b07126.
[43] D.K. Nagesha, X.R. Liang, A.A. Mamedov, G. Gainer, M.A. Eastman, M. Giersig, J.J. Song, T. Ni, N.A. Kotov, In_2S_3 nanocolloids with excitonic emission: In_2S_3 vs CdS comparative study of optical and structural characteristics, J. Phys. Chem. B 31 (2001) 7490–7498, https://doi.org/10.1021/jp011265i.
[44] S.P. Patil, B. Bethi, G.H. Sonawane, V.S. Shrivastava, S. Sonawane, Efficient adsorption and photocatalytic degradation of Rhodamine B dye over Bi_2O_3-bentonite nanocomposites: a kinetic study, J. Ind. Eng. Chem. 34 (2016) 356–363, https://doi.org/10.1016/j.jiec.2015.12.002.
[45] J.Q. Chang, Y. Zhong, C.H. Hu, J.L. Luo, P.G. Wang, Hollow microspheres of BiOCl assembled with nanosheets: Spray drying synthesis and drastically enhanced photocatalytic activity, J. Environ. Chem. Eng. 6 (2018) 6971–6978, https://doi.org/10.1016/j.jece.2018.10.066.
[46] H. Li, F. Xie, W. Li, H. Yang, R. Snyders, M.F. Chen, W.J. Li, Preparation and photocatalytic activity of Ag_2S/ZnS core-shell composites, Catal. Surv. Asia 22 (2018) 156–165, https://doi.org/10.1007/s10563-018-9249-2.
[47] Q.Y. Tian, W. Wu, S.L. Yang, J. Liu, W.J. Yao, F. Ren, C.Z. Jiang, Zinc oxide coating effect for the dye removal and photocatalytic mechanisms of flower-like MoS_2 nanoparticles, Nanoscale Res. Lett. 12 (2017) 221–231, https://doi.org/10.1186/s11671-017-2005-0.
[48] Y.C. Wan, J. Chen, J. Zhan, Y.L. Ma, Facile synthesis of mesoporous $NiCo_2O_4$ fibers with enhanced photocatalytic performance for the degradation of methyl red under visible light irradiation, J. Environ. Chem. Eng. 6 (2018) 6079–6087, https://doi.org/10.1016/j.jece.2018.09.023.
[49] Y.Y. Zhao, L. Kuai, B.Y. Geng, Low-cost and highly efficient composite visible light-driven Ag-AgBr/gamma-$Al2O_3$ plasmonic photocatalyst for degrading organic pollutants, Catal. Sci. Technol. 2 (2012) 1269–1274, https://doi.org/10.1039/c2cy20074k.
[50] S.Y. Dong, J.L. Feng, M.H. Fan, Y.Q. Pi, L.M. Hu, X. Han, M.L. Liu, J.Y. Sun, J.H. Sun, Recent developments in heterogeneous photocatalytic water treatment using visible light-responsive photocatalysts: a review, RSC Adv. 5 (2015) 14610–14630, https://doi.org/10.1039/c4ra13734e.
[51] J. Chen, W.X. Liu, Z.P. Song, H.L. Wang, Y.M. Xie, Photocatalytic degradation of beta-O-4 lignin model compound by In_2S_3 nanoparticles under visible light irradiation, Bioenergy Res. 11 (2018) 166–173, https://doi.org/10.1007/s12155-017-9886-8.